

See discussions, stats, and author profiles for this publication at: <https://www.researchgate.net/publication/266441239>

Local Structure and Dynamics of Lithium Garnet Ionic Conductors: A Model Material Li₅La₃Ta₂O₁₂

ARTICLE *in* CHEMISTRY OF MATERIALS · SEPTEMBER 2014

Impact Factor: 8.35 · DOI: 10.1021/cm502133c

CITATIONS

12

READS

63

4 AUTHORS, INCLUDING:



[Yuxing Wang](#)

Pacific Northwest National Laboratory

7 PUBLICATIONS 76 CITATIONS

[SEE PROFILE](#)



[Wei Lai](#)

Michigan State University

27 PUBLICATIONS 615 CITATIONS

[SEE PROFILE](#)

Local Structure and Dynamics of Lithium Garnet Ionic Conductors: A Model Material $\text{Li}_5\text{La}_3\text{Ta}_2\text{O}_{12}$

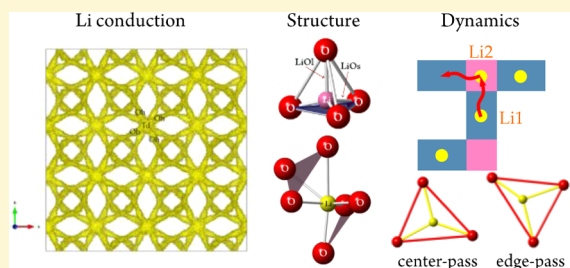
Yuxing Wang,[†] Matthew Klenk,[†] Katharine Page,[‡] and Wei Lai^{*,†}

[†]Department of Chemical Engineering and Materials Science, Michigan State University, East Lansing, Michigan 48824, United States

[‡]Lujan Neutron Scattering Center, Los Alamos National Laboratory, Los Alamos, New Mexico 87545, United States

Supporting Information

ABSTRACT: In this article, we combined two complementary structure/dynamics probes, i.e., total-scattering/reverse Monte Carlo (RMC) modeling and classical molecular dynamics (MD), in order to understand local lithium structure and dynamics in a model disordered garnet oxide $\text{Li}_5\text{La}_3\text{Ta}_2\text{O}_{12}$. By examining the configurations from RMC and trajectories from MD, we individually and statistically analyzed the lithium distribution and dynamics within tetrahedral (Td) cages, octahedral (Oh) cages, and triangular bottlenecks. We found that lithium atoms within either Td or Oh cages prefer to stay at the off-center positions and close to one of the triangular bottlenecks. This is likely caused by the uneven Li–Li interaction in the form of lithium clusters, and such geometrical frustration leads to the local structure instability and fast ionic conduction. Both RMC and MD studies support that the lithium conduction path goes through the triangular bottleneck in a 3D continuous network of Td/Oh cages, without a direct Oh to Oh jump. However, the conduction mechanism should not be generalized, as it is greatly influenced by the local environment or temperature. Broadly speaking, lithium atoms hop through the bottleneck from an edge-passing mechanism at low temperatures to a center-passing mechanism at higher temperatures.



INTRODUCTION

Currently, liquid-based electrolytes with organic solvents have been the primary choice for electrolyte systems in lithium-ion batteries. However, the continued push for high-performance batteries and the application of lithium-ion batteries in electric vehicles call for electrolyte materials with improved safety and stability.^{1–4} Among various solid-state inorganic electrolyte systems, lithium garnet oxides have received wide attention over the past decade due to their good ionic conductivity and electrochemical stability. The majority of research on this materials family has focused on various cation-doping strategies to improve the ionic conductivity.^{5–12} Compounds with bulk conductivities as high as 1 mS/cm have been reported.^{7,8,12}

Many studies in lithium garnet oxides have been devoted to understanding their average structure, by neutron diffraction (ND) and Rietveld refinement (RR), as reviewed by Cussen.¹³ The average structure can be characterized as either cubic with space group $Ia\bar{3}d$ (#230) or tetragonal with space group $I4_1/acd$ (#142, origin 2). The cubic structure has two types of oxygen cages that can be occupied by lithium atoms, i.e., Td-24d (tetrahedrally coordinated) and Oh-48g (octahedrally coordinated). The tetragonal structure has four types of cages, i.e., Td-8a, Td-16e, Oh-16f, and Oh-32g. Td and Oh cages are connected by triangular oxygen faces (named bottlenecks hereafter) in both types of structures. There are three model materials in this garnet family, i.e., $\text{Li}_3\text{Nd}_3\text{Te}_2\text{O}_{12}$ (Li3NT), $\text{Li}_7\text{La}_3\text{Zr}_2\text{O}_{12}$ (Li7LZ), and $\text{Li}_5\text{La}_3\text{Ta}_2\text{O}_{12}$ (LiSLT). Li3NT has a cubic ordered structure in which Td-24d cages are fully

occupied by lithium and Oh-48g cages are fully empty. The second model material, i.e., Li7LZ, has a tetragonal ordered structure at room temperature, in which Td-8a, Oh-16f, and Oh-32g cages are fully occupied by lithium and Td-16e cages are fully empty. The third model material, LiSLT, along with other high-conductivity compositions, has a cubic disordered structure, with both Td-24d and Oh-48g cages partially occupied. The average structure of these disordered materials is characterized by the partial occupancy values in each type of cage and unusually large atomic displacement parameters (ADPs) for the corresponding sites. Due to the application of mean-field parameters such as partial occupancy and its strong correlation with ADPs, information regarding the Li distribution from the average structure can be insufficient or even inaccurate. The actual local positions of Li in the tetrahedral and octahedral cages are still unclear. Furthermore, the average structure gives no information about how Li passes through the bottleneck on the conduction path. Understanding the local structure and dynamics of these disordered cubic materials calls for local probes beyond the ND/RR technique.

Computational modeling provides such a local probe to obtain atomic-scale information of complex materials. Thangadurai et al. studied the migration pathways of $\text{Li}_5\text{La}_3\text{M}_2\text{O}_{12}$ ($\text{M} = \text{Ta}^{5+}, \text{Nb}^{5+}$) with a bond valence sum approach, although they

Received: June 11, 2014

Revised: August 7, 2014



ACS Publications

© XXXX American Chemical Society

A

dx.doi.org/10.1021/cm502133c | Chem. Mater. XXXX, XXX, XXX–XXX

used space groups different from $Ia\bar{3}d$.¹⁴ Adams and Rao were the first to perform classical molecular dynamic (MD) on $Li_{7-x}La_3(Zr_{2-x}M_x)O_{12}$ ($M = Ta^{5+}, Nb^{5+}$, $x = 0, 0.25$) with Morse-type interatomic potentials.¹⁵ Xu et al. studied the structure and transport mechanism in $Li_3La_3Te_2O_{12}$, $Li_5La_3Nb_2O_{12}$, and Li_7LZ , with energy minimization and nudged elastic band (NEB) method based on DFT.¹⁶ Miara et al. studied the stability and ionic conductivity of $Li_{7+2x-y}(La_{3-x}Rb_x)(Zr_{2-y}Ta_y)O_{12}$ ($0 \leq x \leq 0.375$, $0 \leq y \leq 1$) with ab initio molecular dynamic (AIMD) simulations.¹⁷ Phase transition and conduction mechanisms in tetragonal and cubic phases of Li_7LZ were also studied with AIMD by Bernstein et al.,¹⁸ Jalem et al.,¹⁹ and Meier et al.²⁰ We recently studied the potential energy landscape of a $Li_{7-x}La_3(Zr_{2-x}Ta_x)O_{12}$ ($x = 0-2$) series by energy minimization with interatomic potentials.²¹ First, it can be seen that the cubic disordered model material Li5LT has not been thoroughly investigated, although it was first identified as possessing potentials of fast ionic conduction.⁵ Second, due to high computational cost, AIMD simulations on lithium garnets were limited to hundreds of atoms (one unit cell; leading to possible lack of statistical importance) and tens of picoseconds in simulation time (missing information for room temperature). Third, experimental verifications of classical MD and AIMD simulations have been limited to comparison with experimental lattice parameters and ionic conductivities but not with pair distribution functions (PDF), which are essential functions to describe the time-averaged structure of materials.

Total scattering combined with PDF analysis is another local structure probe to obtain the atomic-scale information of complex materials.²²⁻²⁴ On one hand, experimental PDF provides another means to verify MD simulations. On the other hand, reverse Monte Carlo (RMC) modeling of experimental PDF is able to independently extract statistics of local structure features that can be compared with those from MD simulations.²⁵ While the PDF analysis of neutron and X-ray scattering is an established method in the study of liquid and glasses, it has been applied only occasionally to the study of ionic conductors, such as Cu^+ superionic conductor CuI ,²⁶ Ag^+ superionic conductor Ag_2Te ,²⁷ O^{2-} superionic conductor $La_2Mo_2O_9$,²⁵ H^+ superionic conductor Y-doped $BaCeO_3$,²⁶ Li^+ superionic conductor $Li_xLa_{2/3-x/3}TiO_3$,²⁸ and others. To our knowledge, no PDF analysis has been performed on lithium garnets, and no MD simulation has been performed on Li5LT.

In this study, we focused our attention on Li5LT as a model material in order to understand the local structure and dynamics of cubic disordered Li garnets. We combined two complementary local structure/dynamics probes, i.e., total-scattering/RMC and classical MD, in order to understand the local lithium distribution and dynamics in Td-24d cages, Oh-48g cages, and triangular bottlenecks. The article is organized as follows. First, we present the general results of RR and RMC modeling of neutron total-scattering data. Second, we present the comparison of experimental lattice parameters, PDFs, and ionic conductivities with those from MD simulation to demonstrate the validity of interatomic potentials and simulation approaches. Third, we analyze the local structure and dynamic information from independent RMC modeling and MD simulation. This includes occupancy of individual Td/Oh cages, atomic probability density functions (atomic p.d.f.), local lithium positions within Td/Oh cages, local lithium positions relative to nearest-neighbor lithium atoms, atomic mean squared displacements (atomic MSDs), and, finally,

individual and statistical analysis of lithium dynamics. In the end, we briefly comment on our view of advantages and disadvantages of RR, RMC, and MD in studying Li5LT, based on the discussions presented herein.

■ METHODS

Sample Preparation. Powders of $Li_5La_3Ta_2O_{12}$ were prepared by conventional solid-state reaction. Isotopically enriched $^7LiOH \cdot H_2O$ (Cambridge Isotope Laboratories, Inc.) was used as lithium precursors to minimize the neutron absorption effect of 6Li . $^7LiOH \cdot H_2O$ was dried prior to use. La_2O_3 and Ta_2O_5 were used as La and Ta sources. Stoichiometric amounts of powders were mixed with isopropyl alcohol in polyethylene jars with yttria-stabilized-zirconia (YSZ) balls as grinding media. An extra 10% of the lithium precursor was added to compensate for lithium loss during the high-temperature synthesis. Dried powders were fired at 950 °C for 10 h in air in MgO crucibles to minimize Al contamination. To eliminate possible absorption of H_2O and CO_2 , the powder was then heat treated in a tube furnace under constant Ar flow at 750 °C for 2 h and stored in an inert atmosphere immediately thereafter.

Neutron Total-Scattering Experiments and Reverse Monte Carlo Modeling. The neutron total-scattering data were collected at 15, 300, and 550 K by the NPDF instrument at Lujan Neutron Scattering Center, Los Alamos National Laboratory. Around 5 g of powders was sealed in a vanadium container for the sample runs. Separate runs on the empty chamber, empty container, and vanadium-niobium rod were performed for normalization, background, and absorption corrections. The data processing software PDFgetN²⁹ was used to obtain the normalized total-scattering structure function $S(Q)$ and scattering-based atomic pair distribution function (atomic PDF) $G^{PDF}(r)$. The standard definition of $G^{PDF}(r)$ and its relation to $S(Q)$ are given in the Appendix. The choice of maximum Q (momentum transfer) strongly affects the noises in $G^{PDF}(r)$ at low r . A Q_{max} that is too small results in large termination ripples, whereas Q_{max} that is too large increases noise due to the diminishing signal-to-noise ratio in the experimentally collected data at high Q . Therefore, the optimal Q_{max} was determined for each data set by minimizing the quality criterion term G_{low} for the range of $1 \text{ \AA} < r < 1.75 \text{ \AA}$.³⁰ Scale factors were also determined during the process. The effective density was manually adjusted so that $S(Q)$ oscillates around 1 at Q_{max} consistent with the general data reduction practices in the field.

Rietveld refinement was performed using GSAS-EXPGUI^{31,32} (General Structure Analysis System) package to obtain the average structures, which were then used to generate initial configurations for the RMC modeling carried out with the software package RMCProfile.³³ Supercells ($5 \times 5 \times 5$) with lithium atoms randomly distributed at Td-24d and Oh-48g sites were constructed as the initial configuration for each temperature. Minimum distance constraints (in the order of La-La, La-Ta, La-O, Ta-Ta, Ta-O, Li-Li, Li-La, Li-Ta, Li-O, and O-O in units of Å: 3.65, 3.2, 2.2, 5.1, 1.8, 1.95, 2.7, 2.7, 1.7, and 2.4) were applied. These values were chosen to be slightly less than those in the average structure for the same atomic pairs. Similar constraints have been used to study lithium lanthanum titanate.²⁸ The noise in $G(r)$ at low r ($r < 1.75 \text{ \AA}$) was excluded in the fit. Forty separate runs were performed to check the reproducibility of results derived from the stochastic modeling processes and to generate smooth density maps. Structure visualization was enabled by VESTA³⁴ or CrystalMaker.³⁵

Molecular Dynamics Simulation. MD simulations were carried out using the DL_POLY Classic package.³⁶ The atomic interactions were modeled with the same long-range Coulombic potential, short-range Buckingham potential, and Dick-Overhauser core-shell potential for O and Ta atoms, as in our previous study.²¹ The atomic masses of the O shell and Ta shell were set to be 0.2 and 1.0 au, respectively, with a dynamic shell model.³⁷ To calculate the trajectories of the ions, velocity Verlet integration was employed with a time step of 0.25 fs. The optimized $2 \times 2 \times 2$ supercell from our previous energy minimization study was used as the initial configuration.²¹ An initial heating step was performed at 1200 K using NPT ensemble with a

Berendsen thermostat and barostat and relaxation time constants of 0.1 and 0.5 ps, respectively. Subsequent NPT runs at 300, 350, 475, 550, 700, 900, and 1100 K were performed to obtain the lattice parameters. To observe the long-time diffusive properties of lithium, NVE simulations were carried out for 1 ns, and trajectories were saved every 0.1 ps. To sample the fine details of lithium dynamics, additional NVE simulations were carried out at 550 K for 2.5 ps with trajectories saved every 2.5 fs.

Atomic MSDs were calculated according to the standard definition $\langle |\delta r_i(t)|^2 \rangle = 1/N \sum_{i=1}^N \langle |r_i(t) - r_i(0)|^2 \rangle$, which spans from 0 to 500 ps. N is the total number of atoms. A linear fit was performed from 400 to 500 ps to extract self-diffusivity as $D = 1/6 \lim_{t \rightarrow \infty} \langle |\delta r_i(t)|^2 \rangle / t$, i.e., eq A8

in the Appendix. We evaluated the thermodynamic factor Γ numerically from fluctuation of number of particles, i.e., eq A10, in a region that is representatively large (for statistical accuracy) but small compared with the simulation box, as suggested by the recent work of Schenell et al.³⁸ Specifically, we picked center regions of $1/8$ (~ 40 Li atoms) and $1/16$ (~ 20 Li atoms) volume of the $2 \times 2 \times 2$ simulation box and calculated the fluctuation from 500 ps to 1 ns. The final Γ value was averaged from these two regions. The ionic conductivity from MD was calculated using both self-diffusivity and thermodynamic factor according to eq A9.

RESULTS AND DISCUSSION

Average Structure by the Rietveld Refinement. The average structures of Li5LT at three different temperatures, 15, 300, and 550 K, were determined by the Rietveld refinement of the neutron total-scattering data. Ta and La atoms fully occupy octahedrally coordinated sites (16a) and dodecahedrally coordinated sites (24c). Li atoms in the average structure partially occupy the tetrahedral site 24d and octahedral site 48g. The geometric relations of Li tetrahedra and octahedra, i.e., Td and Oh cages, are shown in Figure 1. Each Oh cage is surrounded by two Td cages, and each Td cage is surrounded by four Oh cages (Figure 1a,b). The connection between neighboring Td and Oh cages is the triangular face formed by three oxygen atoms, i.e., bottleneck (Figure 1d). The lithium polyhedra connect to form a continuous 3D network (schematically shown in 2D in Figure 1c).

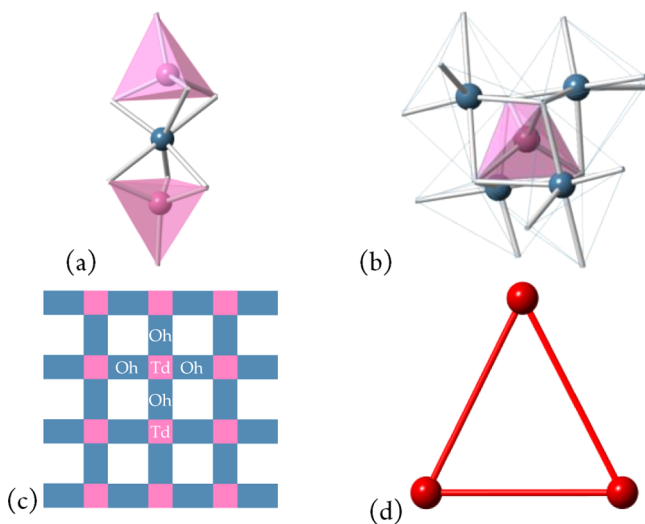


Figure 1. Specific aspects of the average structure of Li5LT. (a) One Li octahedron (Oh) shares faces with two Li tetrahedra (Td). (b) One Li tetrahedron share faces with four Li octahedra. The corner atoms are oxygen in panels a and b. (c) Connectivity of Td and Oh cages shown schematically in 2D. (d) Triangular faces with three oxygen atoms as bottlenecks.

Table 1. Rietveld Refinement Results of $\text{Li}_5\text{La}_3\text{Ta}_2\text{O}_{12}$ ^a Collected at 15, 300, and 550 K Using the Isotropic Model

	15 K	300 K	550 K
lattice parameter (Å)	12.7409(12)	12.7702(12)	12.7989(14)
24d occupancy	0.749(12)	0.757(12)	0.757(15)
48g occupancy	0.458(6)	0.454(6)	0.454(7)
24d 100-U _{iso} (Å ²)	0.026(14)	0.033(1)	0.040(2)
48g 100-U _{iso} (Å ²)	0.046(23)	0.050(2)	0.056(3)

^aSpace group $Ia\bar{3}d$. Anisotropic ADPs (in Å²) at 300 K when anisotropic models were used are as follows: La ($U_{11} = 0.0099$, $U_{22} = U_{33} = 0.0037$, $U_{23} = 0.0023$), Ta ($U_{11} = U_{22} = U_{33} = 0.0026$, $U_{12} = U_{13} = U_{23} = 0.0003$), O ($U_{11} = 0.0089$, $U_{22} = 0.0052$, $U_{33} = 0.0086$, $U_{12} = -0.0002$, $U_{13} = 0.0004$, $U_{23} = -0.0011$), 48g-Li ($U_{11} = 0.1435$, $U_{22} = U_{33} = 0.0167$, $U_{12} = U_{13} = -0.0345$, $U_{23} = -0.0040$).

The relevant refinement results are summarized Table 1. Using a model where the ADPs of all atoms are set to be isotropic, La, Ta, and O atoms have normal values of atomic displacement factors for thermal vibrations of crystalline materials; the ADPs for lithium (Table 1) are unusually large at both sites, characteristic of positional disorder. Using an alternative model where the ADPs of all atoms except 24d-Li are set to be anisotropic, the goodness of fit was greatly improved (from 13.3 to 9.75). All atoms display a certain degree of anisotropy, especially 48g-Li. These structure parameters are similar to those from our previous RR studies with a different neutron diffractometer.²¹

Experimental Total-Scattering Data and RMC Modeling. The normalized total-scattering intensity $S(Q)$ and atomic PDF $G^{\text{PDF}}(r)$ of the 15 K data are shown in Figure 2. Ideally, $S(Q)$ should remain flat at 1 at high Q . In this experiment, the $S(Q)$ value slowly decreases with Q at high Q (inset in Figure 2a). There may be an artificial background present in the whole Q range due to incomplete background and absorption corrections. Fortunately, this kind of artificial background is a

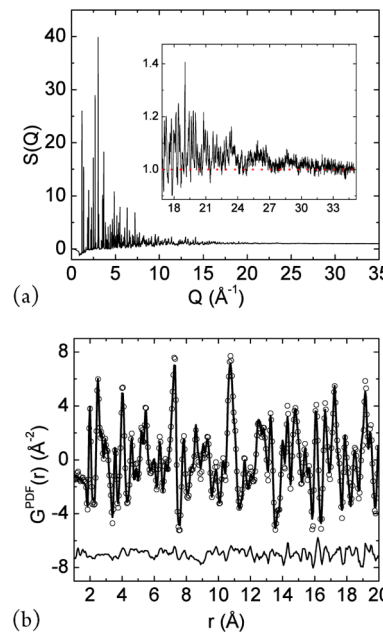


Figure 2. (a) Normalized $S(Q)$ at 15 K. The dotted red line is the baseline to which $S(Q)$ should approach at high Q . (b) Comparison of experimental and fitted $G^{\text{PDF}}(r)$ at 15 K. Experimental data and fitted curves are represented by circle symbols and lines, respectively.

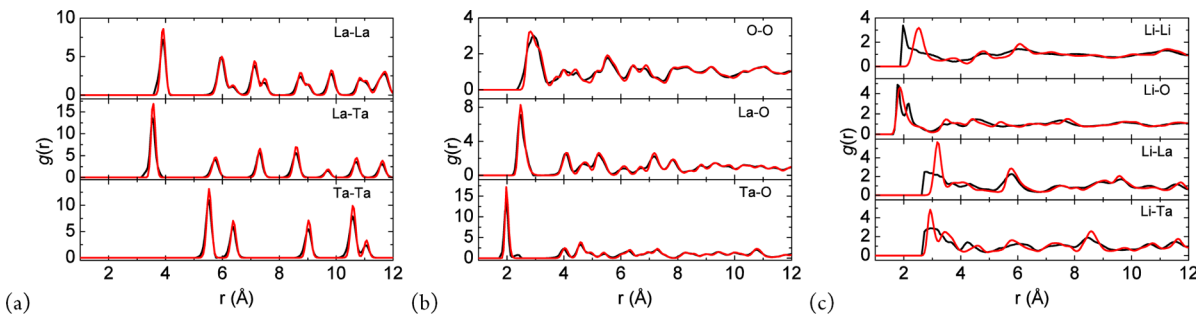


Figure 3. Atomic partial PDFs of (a) pairs containing La and Ta, (b) pairs containing O but no Li, and (c) pairs containing Li at 300 K. Note the separate scales in each graph. (Red color, MD; black color, RMC.)

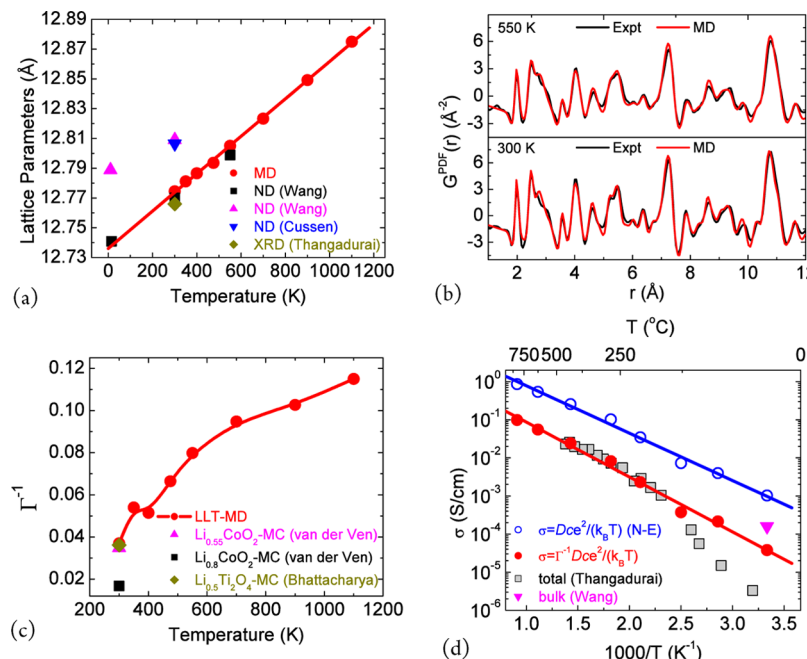


Figure 4. (a) Lattice parameters as a function of temperatures determined by the Rietveld refinement and simulated by MD. Values from ND and XRD studies of Wang,²¹ Cussen,⁴⁰ and Thangadurai⁵ are shown for comparison. (b) Comparison of atomic PDFs $G^{\text{PDF}}(r)$ obtained from total-scattering experiments and from MD simulations at 300 and 550 K. (c) Simulated inverse thermodynamic factors of Li5LT as a function of temperature. (d) Ionic conductivities derived from MD simulation. The experimental values are from Thangadurai⁵ and from our previous work.⁸

slowly varying function of Q that modifies the PDFs only at the low r end where no structural information is contained.

A good fit of the experimental PDFs was achieved for all temperatures (only 15 K data shown in Figure 2) using RMC modeling. There are 22 000 atoms in the model, each having three degrees of freedom. The total number of variables is much larger than the number of data points, so the fitting problem is severely underconstrained, i.e., many solutions satisfy the experimental constraints. Nevertheless, different solutions may contain equivalent structural information if this information is obtained by summation or integration. To check if this is the case, results from 40 separate trials under the same initial conditions were compared. Furthermore, the reliability of the solutions should be judged from the soundness of the physical meanings. In RMC modeling, the fitted partial PDFs were found to be nearly identical for all 40 trials. We obtained the partial PDFs by averaging over all trials and present them in Figure 3, along with those from MD simulation. RMC modeling results are in black, and MD simulation results are in red.

From RMC modeling, partial PDFs involving La and Ta consist of distinct Gaussian-type peaks at both short and long distances, characteristic of long-range ordering in typical crystalline materials. Partial PDFs of pairs involving O atoms exhibit short-range ordering (strong peaks at short distances), and some smaller oscillations around 1 have broader peaks at both short and long distances. The partial PDFs suggest that the structure is composed of solid-like atomic distributions of La/Ta, liquid-like atomic distributions of Li, and intermediate atomic distributions of O. The overall Li5LT structure can be viewed as amorphous lithium phase within a crystalline framework.

Here, we will briefly compare the partial PDFs obtained from RMC and MD. The two techniques yield similar results for pairs not involving Li. Noticeable difference in partial PDFs of Li–Li, Li–O, Li–La, and Li–Ta were observed. This can be understood from the different approaches (stochastic for RMC and deterministic for MD) of these two techniques. RMC modeling is able to access all configurations, consistent with overall $G^{\text{PDF}}(r)$, whereas MD simulation explores the potential energy surface compatible with the kinetic energy. In addition,

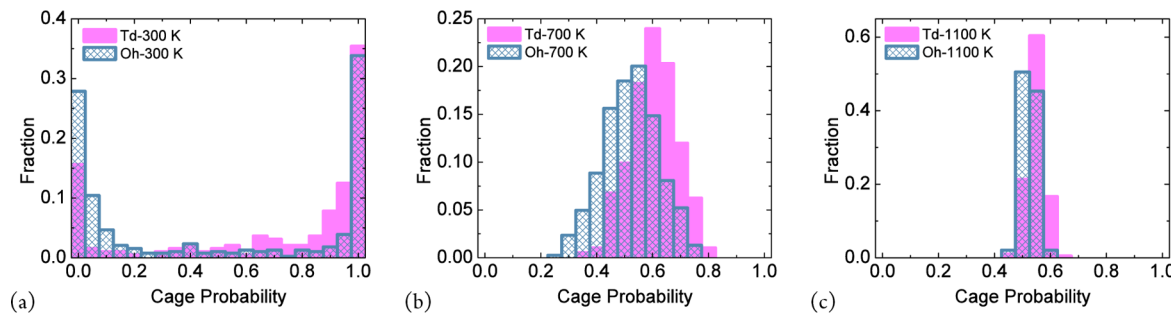


Figure 5. Histograms of probabilities of tetrahedral and octahedral sites being occupied at (a) 300 K, (b) 700 K, and (c) 1100 K, from MD simulation.

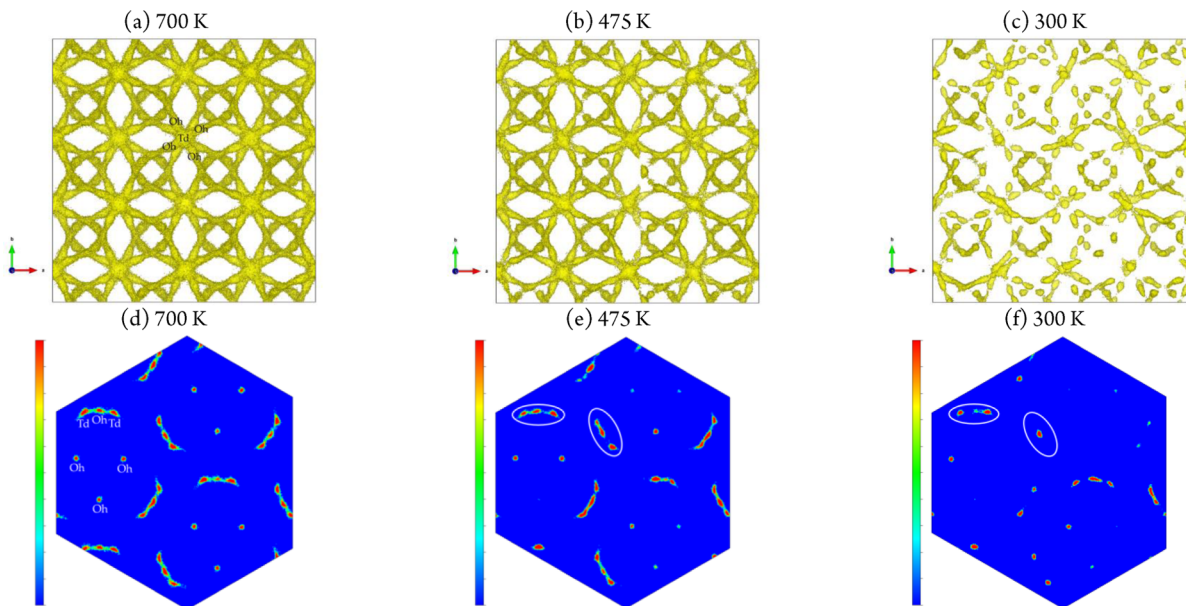


Figure 6. Li nuclear density maps in a $2 \times 2 \times 2$ supercell derived from MD simulation at (a) 700 K, (b) 475 K, and (c) 300 K (isosurface level of 0.1\AA^{-3}). Two-dimensional Li density maps of the (111) plane, with a distance of 23\AA to the origin, cutting through Td-Oh-Td cages at (d) 700 K, (e) 475 K, and (f) 300 K with isosurface levels from 0 to 1\AA^{-3} .

RMC modeling employs a distance constraint, and MD employs a potential “constraint”. Finally, Li has the lowest neutron-scattering length among all atoms in LiSLT (-2.22 fm compared to 8.24 fm for La, 6.91 fm for Ta, and 5.803 fm for O), so pairs involving Li might have slightly higher statistical error. These differences are likely to yield slightly different results from RMC modeling and MD simulation.

Experimental Verification of MD Simulation. First, lattice parameters determined by the Rietveld refinement and MD are in good agreement (Figure 4a), both in terms of the absolute values and the expansion coefficients. Second, the neutron-scattering-based atomic PDFs $G^{\text{PDF}}(r)$ were calculated from partial PDFs of MD simulation, according to eq A3. The simulated patterns are in good agreement with the experimental PDFs (Figure 4b). Similar trends, such as peak broadening with increasing temperature, are observed in both experimental and simulated PDFs. Third, we compared the ionic conductivities calculated from MD and those from experiments by Thangadurai⁵ and our previous work.⁸ As discussed in the Methods section, we used eq A9 in the Appendix, instead of simply using the Nernst–Einstein (N–E) equation, to calculate the ionic conductivity. The underlying assumption of the N–E equation is that the system can be considered as ideal solutions. In LiSLT, the number of mobile ions is on the same scale as the

number of hosts (both tetrahedral and octahedral sites); the mobile ions strongly interact with each other. Therefore, the LiSLT system is nonideal. Values of inverse thermodynamic factors, Γ^{-1} , from different temperatures are shown in Figure 4c. All Γ^{-1} values at different temperatures are well below 1, suggesting strong deviations from the ideal solution conditions. Similar values have been reported for other similar systems such as Li_xCoO_2 and $\text{Li}_x\text{Ti}_2\text{O}_4$, obtained from grand canonical Monte Carlo simulation by van der Ven et al. and Bhattacharya et al.^{21,39} If the thermodynamic factors are not accounted for (just the N–E equation), then the ionic conductivities are overestimated by at least 1 order of magnitude (open blue circles in Figure 4d), similar to what was observed from AIMD simulation.¹⁹ After the thermodynamic factors are accounted for, the simulated ionic conductivities are in good agreement with the experimental data from Thangadurai et al.⁵ and from us.⁸ Since the experimental data⁵ are the total conductivity values and our simulated values are for the bulk conduction, the discrepancy at low temperatures can be attributed to the grain boundary resistances.

Comparison of lattice parameters, atomic PDFs, and ionic conductivities at different temperatures shows a good match between MD simulation and experimental values. This demonstrates that our interatomic potential models are

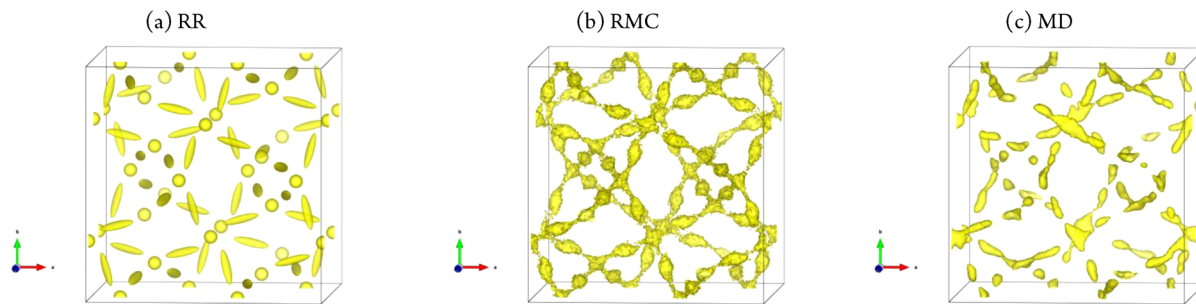


Figure 7. Nuclear density maps of Li in a $1 \times 1 \times 1$ cell at 300 K derived from (a) RR, (b) RMC modeling, and (c) MD. Isosurface level of 0.5 \AA^{-3} .

sufficiently accurate and simulation approaches are appropriate. Next, we will present our analysis of local structure and dynamics from MD simulation and compare it with information from RMC modeling, when available.

Occupancy of Individual Td/Oh Cages. The Li dynamics and site stabilities can be inferred by examining the occupancy evolution over a period of time in MD (500 ps to 1 ns) for individual cages. For instance, by tracking the binary occupation information (1 for occupied or 0 for empty) of particular cages for a period of time, we determined the accumulated times (normalized to the total time) of the sites being occupied, defined as the probabilities of the cages being occupied. The Td cages are defined as a spherical region with a radius of 0.65 Å centered at the 24d positions, whereas Oh cages have a radius of 1.4 Å centered at the 48g positions. The radii were chosen so that the occupancy sum of the two types of cages is roughly 1 (not rigorously 1). Figure 5 shows the histograms of the probabilities for Td and Oh cages. At 300 K, it was clear that most cages were either occupied or empty (bimodal) for a majority of the time regardless of whether it was Td or Oh. Comparatively, the histograms at 700 K indicate that the occupancies of most cages varied with time, so probabilities with high occurrence were 0.6 and 0.5 for the Td and Oh cages, respectively. The histogram of cage probability exhibits a normal distribution. At even higher temperature, e.g., 1100 K, the distribution becomes narrower and the average occupancies of two types of cages become similar. The evolution of probability histogram is indicative of increasing Li mobility with temperature, and the fact that the histogram evolution of Td and Oh cages are in sync suggests that tetrahedral and octahedral Li play equally important roles in Li conduction, especially at high temperatures.

Atomic p.d.f. (Nuclear Density Maps) of Li. Nuclear density maps facilitate the visualization of the distribution of atoms. Briefly, the cell is divided into cubic pixels of roughly 0.1 Å in length. The probability density of each type of atom in each pixel is then calculated. Figure 6 compares the Li nuclear density maps in 3D and 2D at 300, 475, and 700 K. In 3D, isosurfaces with a level of 0.1 \AA^{-3} were plotted. In 2D, projections of a (111) plane with a distance of ~ 23 Å to the origin were plotted. At 700 K, density regions within Td and Oh cages connect to form a continuous 3D network, which represents the conduction path of this system (Figure 6a). No nuclear density was observed between the adjacent octahedra, which eliminates the possibility of direct jumping between octahedral cages. The connection of Td and Oh regions, in the form of Td-Oh-Td, can also be visualized from 2D plane projections (Figure 6d). At 300 K, multiple regions of missing density were observed in both 3D and 2D plots (Figure 6c,f). Due to the low transport activity at this temperature, we think

some regions were never accessed by Li during the whole simulation time. At 475 K, almost all Td and Oh regions were connected, but some regions were accessed more than others.

Figure 7 compares the Li density isosurfaces in a $1 \times 1 \times 1$ cell in 3D, as determined by RR, RMC, and MD at 300 K. In the Rietveld refinement, anisotropic ADPs were used for all atoms except Li in Td-24d cages. For the Rietveld refinement, only the Gaussian/harmonic (isotropic or anisotropic) type of density distribution is allowed. The ellipsoids within octahedral regions approximately elongate toward adjacent tetrahedral sites. In comparison, shapes of nuclear density regions within Li tetrahedra and octahedra derived from RMC modeling show much greater complexity. Tetrahedral Li regions have four fingers sticking out toward the triangular faces. This type of nuclear distribution can neither be explained by thermal vibration nor modeled by simple Gaussian distribution. Instead, it reflects complex positional disorder as a result of interaction with its environment.

Lithium atoms in Td cages from MD seem to have a flatter density region than those from RMC, as can be seen from both the $1 \times 1 \times 1$ and $2 \times 2 \times 2$ cells. Furthermore, Oh regions in MD are more cylindrical compared with those in RMC. Such differences can again be understood from the constraint applied in RMC and MD. In RMC, the main constraint is the distance constraint. This is likely to yield a higher probability of lithium in different locations of Oh cages because they are larger than Td cages. In MD, the constraint is the interatomic potential, which has a more delicate influence on the distribution of lithium. From examination of RMC and MD density maps at 3D and 2D, we conclude that the conduction path involves direct hopping between tetrahedral and octahedral cages, consistent with arguments from previous studies for Li₇LZ. ^{15–17,19,41} However, it differs from the proposed direct Oh–Oh jump mechanism studied by Xu et al. with the NEB method¹⁰ for a similar material, Li₅La₃Nb₂O₁₂. This indicates one of the possible shortcomings of applying the NEB method to studying the transport mechanism in highly disordered materials, as a large number of initial and final configurations are possible. The density maps in Figures 6 and 7 are also similar to, but differ in details from, those in Li₅LT studied by the bond valence sum approach.¹⁴ In that study, the pathway is characterized by the nonplanar squares formed by octahedral Li with an almost empty tetrahedral center.

In addition to visualization of atomic p.d.f. with 3D and 2D plots, integration of atomic p.d.f. (p_i) in different regions offers ways to quantify the lithium distribution. For example, a Shannon's configuration entropy can be defined as $S = -\sum_i p_i \ln p_i$, where the summation is over the whole $2 \times 2 \times 2$ cell in Figure 6. Configuration entropies at different temperatures are shown in Figure 8a. Such entropies have larger values at higher

temperatures, reflecting a more dispersed distribution of lithium atoms.

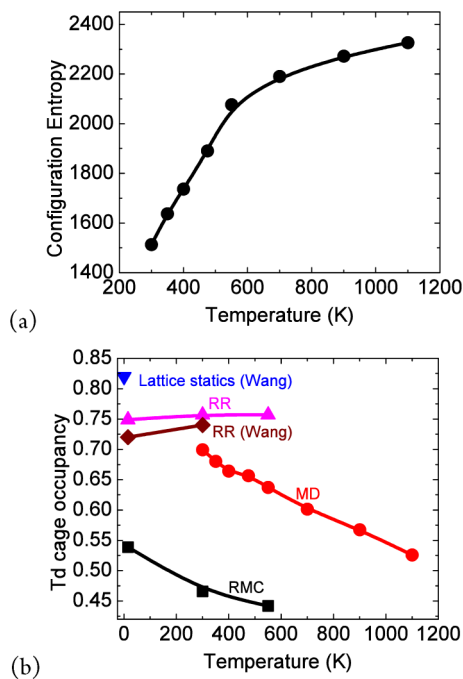


Figure 8. Integration of atomic p.d.f.. (a) Shannon's configuration entropy at different temperatures. (b) Td cage occupancies determined by RR, RMC, MD of the present work and by RR and lattice statics from our previous work.²¹

Another way to quantify lithium distribution is to integrate atomic p.d.f. around all Td or Oh cages to yield Td and Oh cage occupancy values. Here, we obtained three sets of cage occupancies: one from Rietveld refinement of total-scattering data (Table 1) and the other two by RMC modeling and MD. Figure 8 compares the Td cage occupancies using the three techniques. The discrepancies are significant. The Rietveld refinement gave the highest tetrahedral cage occupancies, which are largely temperature-independent. Results from our previous work with a different neutron diffractometer are also shown.²¹ Td cage occupancies determined by MD are slightly lower, and a negative correlation with temperature was observed. It is expected that the tetrahedral site has lower site energies compared with those of the octahedral site due to its higher symmetry. At low temperatures, the tetrahedral sites are preferred; at high temperature, the preference is offset by thermal agitation and lithium atoms tend to have more uniform

distribution. Such negative correlation is in contrast to the positive correlation found in Li₇LZ by Adams and Rao.¹⁵ It is interesting to note that extrapolation of data points in MD to 0 K gave a similar value to that obtained from our previous lattice statics study (energy minimization).²¹ The occupancies determined by RMC modeling are clearly lower than those from MD, but they have a similar negative correlation with temperature. Such lower Td cage occupancy, or higher Oh cage occupancy, is consistent with comparison of RMC and MD density maps in Figure 7 and can be explained in a similar fashion.

Density maps of La, Ta, O atoms from RR, RMC, and MD are shown in Figure S1 in the Supporting Information. Unlike the lithium density maps, these density maps agree fairly well among all three techniques. In contrast to the Ta densities, which are roughly spherical, the La densities derived from the RR and RMC show considerable elongations in certain directions. The O density derived from RMC modeling appears to be quite dispersed, reflecting some degree of disorder.

Local Lithium Positions Relative to Td/Oh Cages. After examining the Td/Oh cage occupancy and lithium p.d.f., we think more insight can be gained by looking at local lithium positions relative to the Td/Oh cages. From average structure studies,¹³ two positions (48g or blue sphere in Figure 9a and 96h or yellow sphere in Figure 9a) have been assigned to the octahedral Li. Only one position (24d) has been assigned to the tetrahedral Li, which is at the geometric center of the Li tetrahedron, as shown in Figure 9a. It is worth noting that the two 96 positions correspond to the anisotropic 48g distribution in Table 1.

We inspected the optimized RMC models to study the local lithium positions inside Td/Oh cages. The typical Li tetrahedra and octahedra are shown in Figure 9b. The tetrahedral Li moves toward the center of the face, resulting in three short Li–O bonds (denoted as LiOs) and one long Li–O bond (LiOl). The average bond distances of the LiOs and LiOl bonds in RMC models at 300 K are 1.86 and 2.15 Å, respectively. Similarly, the octahedral Li prefers to stay close to one of the triangular faces (shaded faces), resulting in the shortening of three Li–O bonds and elongation of the other three Li–O bonds. The Li displacement toward the triangular faces is also evident from statistical analysis of lithium to the closest-face distances. Figure 10 shows the distribution of Li-to-face distances for tetrahedral Li obtained from RMC modeling, MD simulation, and average structure. According to the average structure, tetrahedral Li is at the geometric center of the tetrahedron (24d site) with harmonic motion. We simulated the Li-to-face distance distribution using atomic displacement parameters (U_{iso} of Li: 0.033 Å² and of O: 0.0076 Å² at 300 K)

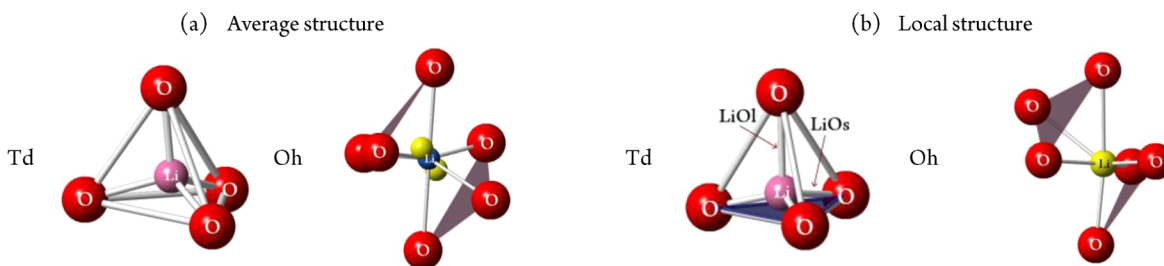


Figure 9. (a) Occupied Td and Oh cage in the average structure determined by RR. The blue sphere is lithium at the 48g position, and the two yellow spheres are lithium at the 96h position. The two triangular bottlenecks are shaded. (b) Occupied Td and Oh cages in the local structure determined by RMC.

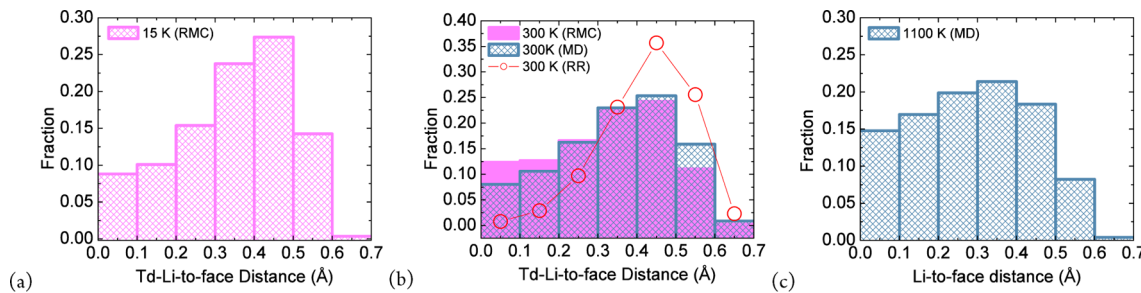


Figure 10. Fractions of Li as a function of the shortest distances between Li and triangular faces by RMC modeling and MD at (a) 15 K, (b) 300 K, and (c) 1100 K.

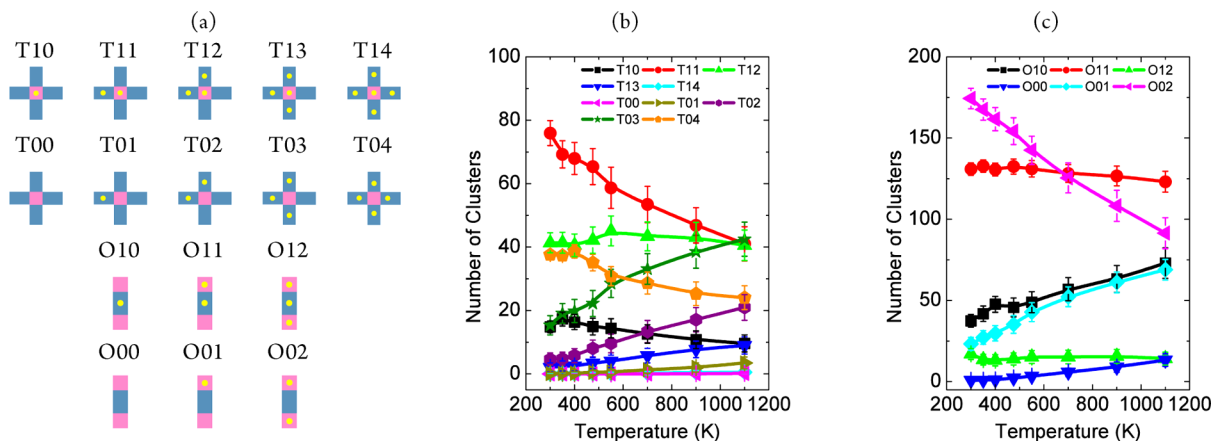


Figure 11. (a) Schematic illustration of all 16 types of Li clusters for cubic garnet systems. Td and Oh cages are represented by pink square and blue rectangles, respectively. Temperature dependence of clusters for (b) the T_{xx} series and (c) O_{xx} series from MD simulations.

determined by Rietveld refinement (Figure 10b). The distance distribution has a peak around 0.45 Å, with a sharp tail and slow tail at long and short distances, respectively. Such shape is the result of overlapping harmonic distribution of both Li and O atoms. The distribution of Li of the local structure from MD and RMC further shifts toward the O faces, confirming the tetrahedral Li displacement. This observation of tetrahedral Li displacement is consistent with energy minimization studies by us²¹ and Xu et al.¹⁶ The displacement is more pronounced as temperature increases, which can be seen from the increasing fractions of Li with short Li-to-face distances (from 15 to 300 K in RMC or from 300 to 1100 K in MD). A small portion of Li is essentially on the triangular face (distance close to 0 Å), so the coordination number should best be considered as three rather than four.

For Li octahedra, according to the average structure, the distances between the 48g site and the two shaded triangles are both 1.29 Å. According to the RMC models, the distances between octahedral Li and the two shaded faces are 1.00 and 1.60 Å for the 300 K data, indicating that the octahedral Li prefers to stay close to one of two faces. The finding regarding the Li displacement from RMC modeling was confirmed by our MD simulation. The average distances between octahedral Li and the two shared O faces are 0.98 and 1.56 Å, agreeing well with the RMC modeling. The origin of the tetrahedral Li shift can be deduced by considering the interaction with neighboring Li atoms. As an occupied Li tetrahedron is surrounded by four partially filled octahedral sites, the ideal tetrahedral symmetry does not hold locally and the uneven Li–Li interactions causes displacements of Li away from the center of the tetrahedron. The displacement of octahedral Li can be explained similarly.

Thus, lithium in both Td and Oh cages is best described as being at the 96h position, from the perspective of average structure, although it is difficult to place lithium at 96h inside a Td cage with just the Rietveld refinement.²¹ Such uneven Li–Li interactions lead to local structure instability and fast ionic conduction, and they can be visualized from the following discussions on lithium clusters.

Local Lithium Positions Relative to Nearest-Neighbor Lithium Atoms (Li Clusters). It is expected that the Li–Li interaction plays a pivotal role in determining the distribution of Li in lithium garnet oxides. By looking at the partial PDF of Li–Li pairs in Figure 3, we recognize that the Li–Li interaction is short-ranged. We will define a total of 16 types of clusters that include 5 occupied Td clusters (T1x), 5 empty Td clusters (T0x), 3 occupied Oh clusters (O1x), and 3 empty Oh clusters (O0x). We use 1 or 0 to show whether the center of the cluster is occupied or empty, respectively, and x is used to represent the number of lithium atoms around the cluster center. Schematics of these 16 clusters are shown in Figure 11a. It is expected that each cluster is associated with a unique potential energy and that the exact conduction path of a hopping event is decided by the type of clusters that the hopping Li belongs to at the initial and final states.

We calculated the average number of each type of clusters at all temperatures in MD simulations (Figure 11b,c). At a particular temperature, the number of each type of cluster fluctuates with time. The error bars represent the standard deviation of each type of cluster for the simulation time from 500 ps to 1 ns. At 300 K, T11 and T12 are common among all T1x clusters, whereas T03 and T04 are common among all T0x clusters. This suggests that the system minimizes the total Li–

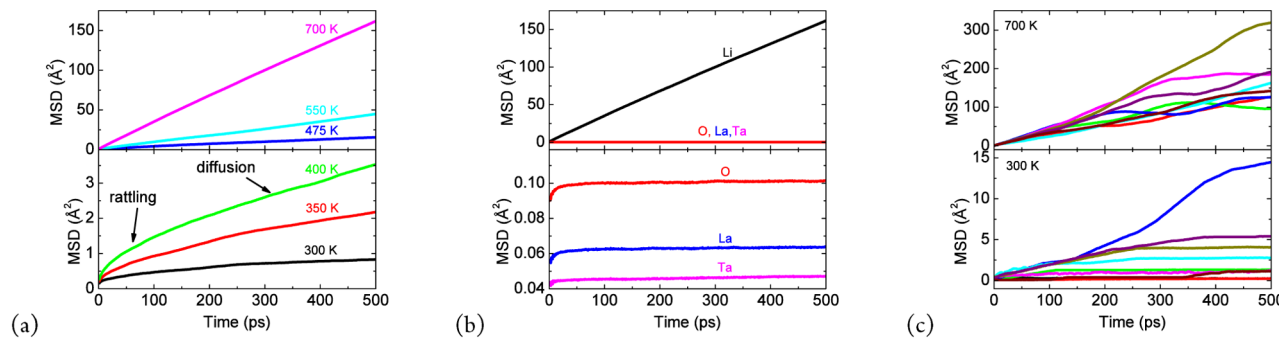


Figure 12. (a) Atomic MSD of Li averaged over all lithium atoms at different temperatures. (b) Comparison of atomic MSD averaged over all lithium and framework atoms at 700 K. (c) MSD of selected lithium atoms at 300 and 700 K.

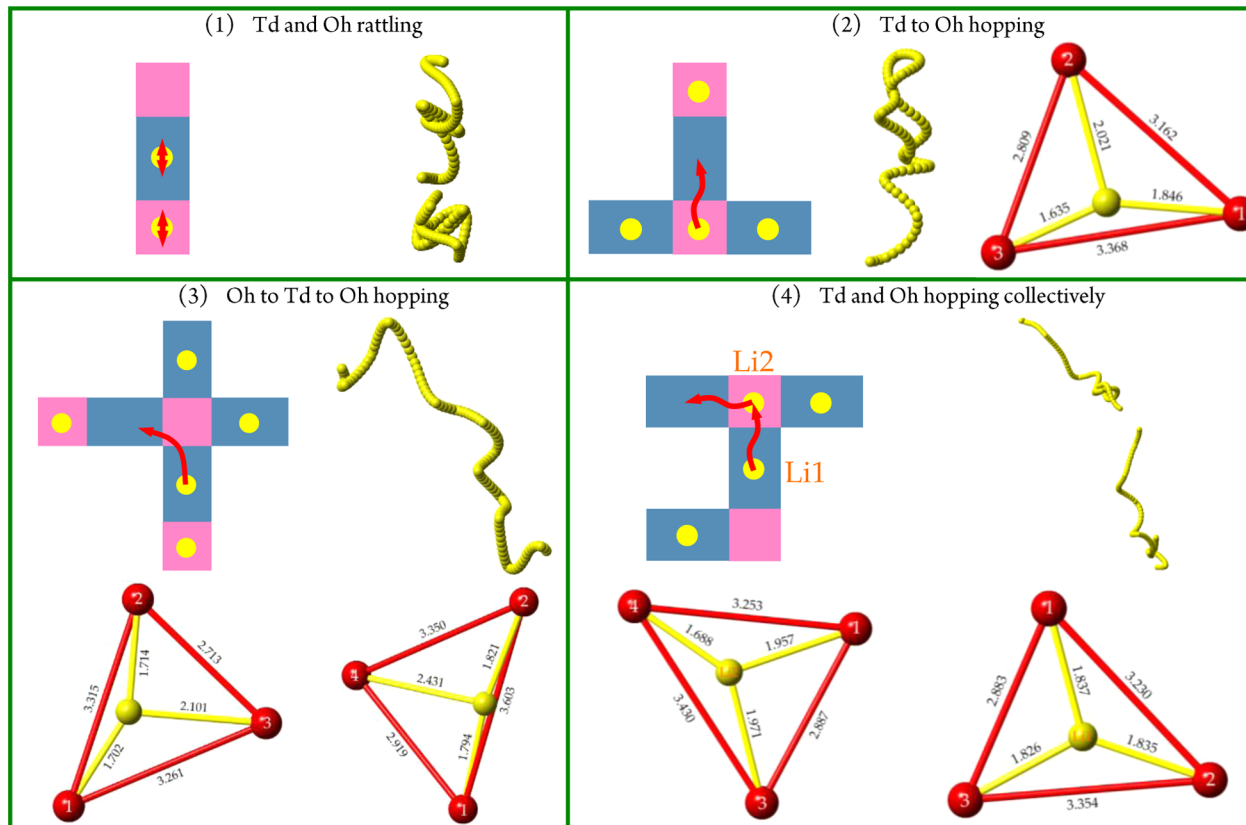


Figure 13. Examples of dynamical events (550 K). In each example, the local environment, Li trajectories, and geometries of bottlenecks as Li goes through the faces are illustrated. Yellow circles represent Li ions. Pink squares and blue rectangles schematically represent Td and Oh cages, respectively.

Li interaction by maximizing the number of octahedral Li around an empty Td cage and minimizing the number of octahedral Li around an occupied Td cage. For the same reason, T14 and T00 clusters have the lowest probability of occurrence. First, both T11 and T12 are asymmetrical clusters that lead to uneven Li–Li interactions, possibly causing lithium atoms to take off-center positions within Td cages, as discussed in Figures 9 and 10. The existence of such uneven Li–Li interactions at low temperatures indicates the local structure instability and could be the origin of fast ionic conduction. Second, the temperature dependence of clusters shows that the distributions of these clusters become more uniform at elevated temperatures. Notable changes are the increasing population of T03 and T02 clusters and decreasing population of T11 and T04. In addition, fluctuations of clusters are related to hopping

events, so the degrees of fluctuation indirectly indicate the stability of each type of cluster. It is not surprising that all clusters become almost equally mobile at high temperatures (with large error bars). We have focused our discussion on the Txx clusters, and the trend in Oxx clusters can be explained similarly.

Atomic MSD. The atomic MSDs of Li averaged over all lithium atoms in the cell are shown in Figure 12a as a function of temperature from the MD simulations. At the long-time limit, the MSD grows linearly with time, suggesting diffusive behavior. As stated in the Methods section, the linear portion from 400 to 500 ps was used to extract the self-diffusivity. At low temperatures, the time dependence of the MSD exhibits subdiffusive or rattling behavior. It can take several hundred picoseconds before it reaches the diffusive regime for low

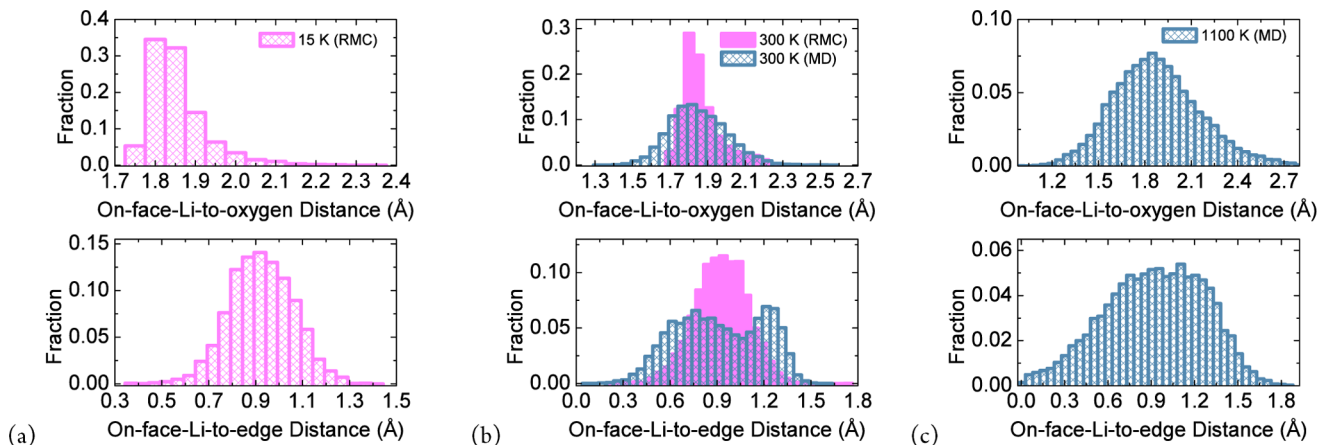


Figure 14. Histograms of the distances of Li to the closest O edge as Li goes through the bottlenecks at (a) 15 K, (b) 300 K, and (c) 1100 K by RMC modeling and MD simulation.

temperatures of 300 and 350 K. This demonstrates the advantage of classical MD over AIMD in studying dynamics at low temperatures. The dynamics of other atoms can be studied by plotting their MSD as a function of time at 700 K (Figure 12b). Unsurprisingly, La, Ta, and O atoms exhibit oscillatory behavior typical of crystalline materials, confirming that they form the rigid framework in which Li atoms diffuse. This is consistent with the picture revealed by partial PDFs in Figure 3.

An interesting feature with regard to Li movement is revealed as the MSDs of individual Li atoms are tracked (Figure 12c, showing only selected lithium atoms). The individual Li MSDs are nonlinear with time. At 300 K, most Li has low mobility, whereas some Li is highly mobile, contributing greatly to the overall MSD. Essentially, the Li transport is dominated by a few fast-moving Li, especially at low temperatures. We believe that the difference in individual Li MSD arises from the distinct local environments of Li, i.e., lithium clusters discussed previously. At high temperatures (e.g., 700 K), more lithium atoms are diffusing and the distribution of Li mobility is more uniform.

Individual and Statistical Analysis of Lithium Dynamics. The local environments of Li in Li₅LT are quite complicated, and dynamics of Li atoms are determined by the local environment (clusters). It is difficult to generalize a universal conduction mechanism. However, three general principles can be inferred from the dynamical events: (1) If Li hops, then it goes through the triangular bottlenecks between Td and Oh cages, (2) some Li movements are correlated, and (3) the oxygen cages have great flexibility to accommodate Li movement. We demonstrate dynamics schematics, lithium trajectories, and bottleneck information with four examples in Figure 13. Lithium trajectories in the form of connected spheres correspond to the motion shown schematically with arrows. The time duration of each example was around 250 fs. Movies of these events can be found in the Supporting Information. Note that events shown in these examples are common but do not exhaust all possible scenarios.

In example 1, i.e., Td and Oh rattling, the two Li atoms never escaped their cages and moved in a correlated fashion, so the Li–Li distance remained largely constant. The trajectories of Li atoms indicate that a large volume within the Oh cages was accessible to Li. In the language of lithium clusters, this example corresponds to an unchanging O₁₁ cluster. In example 2, i.e.,

Td to Oh hopping (O₀₂ to O₁₁ cluster), Li originally in a Td cage did not go through the center of the bottleneck. Rather, it moved close to the edge that is shared with an unoccupied Oh cage. This demonstrates the effects of the local environment on the exact path of Li hopping. Similar trajectories were reported on another composition, i.e., Li₇LZ, by Xu et al.¹⁶ However, the direct jumps between Oh cages proposed by the same authors for Li₅La₃Nb₂O₁₂, which is expected to have very similar conduction behaviors as those of Li₅LT, were not observed in our MD simulation. This was also discussed before in the section on lithium density maps. The similar edge pass-type mechanism was proposed by Jalem et al.¹⁹ at 1273 K for Li₇LZ and was observed by Miara et al.¹⁷ In example 3, i.e., Oh to Td to Oh hopping (O₀₃ to another O₀₃ cluster), Li first went through one bottleneck but stayed close to the edge that is away from the two occupied octahedra. Li proceeded to jump to the neighboring empty Oh cage immediately through the same edge, indicating that the center of the Td cage was not accessed. Looking at the bottlenecks, both events correspond to the edge-passing mechanism. At the second bottleneck, the hopping lithium was so close to the edge that it was almost situated at the center of the edge, accompanied with one long O–O distance (3.6 Å) and one long Li–O distance (2.4 Å). In the last example (O₁₂ to another O₁₂ cluster), two Li atoms in Td and Oh cages hopped synchronously, i.e., the Li originally in a Td cage (Li₂) hopped to an empty Oh cage as Li originally in an Oh cage (Li₁) took the place of the position of Li₂. This collective motion of Li is consistent with Meier's AIMD calculations on the Li₇LZ.²⁰ Interestingly, Li₁ went through the center of the bottleneck, violating the edge-passing mechanism.

To statistically understand how Li atoms pass through the triangular bottlenecks in the hopping events, we captured the Li location on the bottleneck for a simulation time between 900 ps to 1 ns in MD and for all configurations in RMC (more than 1000 lithium atoms in either technique). Specifically, we calculated the distance of Li to three oxygen atoms, denoted as on-face-Li-to-oxygen distances, and to three edges, denoted as on-face-Li-to-edge distances (Figure 14). At 300 K, the average Li–O distances are 1.8 Å according to both MD and RMC modeling, but the distribution of Li–O distances is broader in MD than that in RMC models. The large Li–O distances in the MD distribution (long tails) correspond to edge-passing examples in Figure 13. For the Li-to-edge distances, a bimodal distribution was observed from MD simulation. The first peak

is roughly twice the width of the second peak. To understand this, we again refer to Figure 13. All bottlenecks have two long edges (around 3.3 Å) and one short edge (around 2.8 Å). For the edge-passing mechanism, the Li atoms are closer to the two long edges than to the short edges. This configuration prevents short Li–O distances. The bimodal distribution was not observed in the RMC models, and the distribution suggests a center-passing mechanism. RMC results at 15 K suggest a similar center-passing mechanism. Again, because the distance constraint was used in RMC modeling, we expect that the Li–O distance distribution is narrower and that this bottleneck study will be biased to a center-passing pathway. As the temperature is increased to 1100 K (MD), both the Li–O and Li–edge distance distributions become more spread out, suggesting an overall center-passing mechanism but with many edge-passing events as well. To summarize, we found that the exact Li dynamics and conduction mechanism should not be generalized but are rather determined by the local environment and temperature.

RR vs RMC vs MD. In the end, we will briefly compare the advantages and disadvantages of three techniques discussed in herein, i.e., RR, RMC, MD, in studying the model disordered material LiSLT. RR of conventional neutron diffraction data is the easiest to perform among the three techniques. It is able to qualitatively identify fast ionic conduction (partial occupancy and larger ADPs at two different sites) and can even reveal the conduction path (with anisotropic ADPs), as shown in Figure 7. However, it cannot supply information on the bottleneck since atomic p.d.f. was assumed to be localized as Gaussian a priori. In addition, it is difficult to detect the local structure of high symmetry sites, i.e., a Td cage, with RR due to the enforced symmetry elements. Finally, quantification of site occupancy becomes questionable due to the correlation of occupancy and ADPs.

RMC modeling requires normalized scattering data that call for high signal-to-noise ratio diffractometers and special data processing. RMC modeling can also be severely underconstrained. However, RMC modeling does not require specific potential models, whether they are empirical interatomic potentials or DFT pseudopotentials or functionals, which makes this technique more universally applicable. In addition, RMC modeling can be applied at low temperatures that generally cannot be studied by MD.

MD simulation provides both the temporal and spatial information of the material, but it depends on the accuracy of the potential models. Comparison of MD simulation results with different experimental structure/dynamics probes will help to establish the validity of simulation results.

■ CONCLUSIONS

We combined two complementary local structure/dynamics probes, i.e., total-scattering/RMC and classical MD, in order to understand the local lithium distribution and dynamics in a model lithium garnet oxide, $\text{Li}_5\text{La}_3\text{Ta}_2\text{O}_{12}$. The two techniques validate and complement each other. Experimental lattice parameters, structure functions, and ionic conductivities match well with those from MD simulations.

By tracking the movement of individual Li atoms and occupancy of individual Td/Oh cages, we discovered that there is great disparity in mobility of different atoms and disparity in cage occupancy, especially at low temperatures. In addition, lithium atoms are found to be generally off-center inside Td/Oh cages, which may be attributed to a local environment

effect, e.g., lithium clusters. Our studies support that the lithium conduction path goes through the triangular bottleneck in a 3D continuous network of Td/Oh cages, without a direct Oh to Oh jump. We found that the conduction mechanism should not be generalized, as it is greatly influenced by the local environment and temperature. Broadly speaking, lithium atoms hop through the bottleneck from an edge-passing mechanism at low temperatures to a center-passing mechanism at higher temperatures.

■ APPENDIX

Definitions of Different Pair Distribution Functions

The atomic pair distribution function (atomic PDF) of a material can be calculated given the complete structural information. The partial atomic PDF $g_{ij}(r)$ is defined as

$$g_{ij}(r) = n_{ij}/(4\pi r^2 dr c_j \rho_0) \quad (\text{A1})$$

where n_{ij} is the average number of type j atoms within a shell of r to $r + dr$ centered at a type i atom; ρ_0 is the total number density of all atoms; c_j is the number concentration of type j atoms.

The neutron-scattering-based atomic PDF (denoted $G'(r)$)⁴² is the summation of partial PDFs for all pairs weighted by the concentration and scattering powers of the atom pairs

$$G'(r) = \sum_{i,j=1}^n w_{ij} g_{ij}(r) = \sum_{i,j=1}^n c_i c_j b_i b_j / \left(\sum_{i=1}^n c_i b_i \right)^2 g_{ij}(r) \quad (\text{A2})$$

where b_i is the bound coherent scattering length of type i atom in the case of neutron scattering. n is the number of atomic types. The form of PDF used in the data reduction software PDFgetN (denoted $G^{\text{PDF}}(r)$) is related to $G'(r)$ as

$$G^{\text{PDF}}(r) = 4\pi r \rho_0 [G'(r) - 1] \quad (\text{A3})$$

whereas the form of PDF used in RMC modeling software RMCProfile (denoted $G(r)$) is related to $G'(r)$ as

$$G(r) = \left(\sum_{i=1}^n c_i b_i \right)^2 [G'(r) - 1] \quad (\text{A4})$$

Experimentally, the pair distribution function $G^{\text{PDF}}(r)$ is related to the normalized total-scattering function $S(Q)$ by the Fourier transform

$$G^{\text{PDF}}(r) = \frac{2}{\pi} \int_0^\infty Q [S(Q) - 1] \sin(Qr) dQ \quad (\text{A5})$$

Thermodynamic Factors

From the phenomenological definition of flux and linear irreversible thermodynamics (LIT), the flux J is related to the concentration c and gradient of chemical potential μ by the mobility b^μ as

$$J = -cb^\mu \nabla \mu \quad (\text{A6})$$

Another LIT expression, Ohm's law, relates the flux of charge carriers (charge $z_i e$) to the gradient of electrical potential ϕ by the electrical conductivity σ as

$$J = -(\sigma/z_i e) \nabla \phi \quad (\text{A7})$$

The Einstein relation relates the MSD to the self-diffusivity D in Fick's 1st law as

$$D = \lim_{t \rightarrow \infty} \langle |\delta r_i(t)|^2 \rangle / (6t) = -J / \nabla c \quad (\text{A8})$$

If we assume that the proportionality constants under chemical potential gradient $\nabla\mu$ and electrical energy $\nabla(z_i e \phi)$ are the same, i.e., small-signal approximation, then the combination of all three above equations connects the electrical conductivity to diffusivity by the thermodynamic factor Γ as

$$\sigma = \Gamma^{-1} (z_i e)^2 D_c / (k_B T) \quad (\text{A9})$$

The thermodynamic factor can be evaluated from thermodynamics or fluctuation of number of particles as

$$\Gamma = (\partial\mu/\partial \ln N)_{T,V}/(k_B T) = \langle N \rangle / \sigma_N^2 \quad (\text{A10})$$

where N is the number of particles. Equation A9 reduces to the conventional Nernst–Einstein equation for $\Gamma = 1$, which indicates dilute non-interacting systems ($\mu \sim \mu_0 + k_B T \ln N$) or Gaussian statistics ($\sigma_N = \langle N \rangle^{1/2}$), e.g., for ideal gases.

■ ASSOCIATED CONTENT

Supporting Information

Nuclear density maps of La, Ta, O atoms at 300 K from RR, RMC, and MD results. Movies of atomic dynamics of four examples in Figure 13. This material is available free of charge via the Internet at <http://pubs.acs.org>.

■ AUTHOR INFORMATION

Corresponding Author

*Tel: 001-517-355-5126. Fax: 001-517-432-1105. E-mail: laiwei@msu.edu.

Notes

The authors declare no competing financial interest.

■ ACKNOWLEDGMENTS

We wish to acknowledge the Michigan State University High Performance Computing Center and the Institute for Cyber-Enabled Research for access to their computing resources. This work has benefited from the use of NPDF at the Lujan Center at Los Alamos Neutron Science Center, which was funded by DOE Office of Basic Energy Sciences at the time of measurement. Los Alamos National Laboratory is operated by Los Alamos National Security LLC under DOE contract DE-AC52-06NA25396. We acknowledge the financial support by the Ceramics Program of the National Science Foundation (DMR-1206356).

■ REFERENCES

- (1) Tarascon, J. M.; Armand, M. *Nature* **2001**, *414*, 359–367.
- (2) Armand, M.; Tarascon, J. M. *Nature* **2008**, *451*, 652–657.
- (3) Goodenough, J. B.; Kim, Y. *Chem. Mater.* **2010**, *22*, 587–603.
- (4) Scrosati, B.; Garche, J. *J. Power Sources* **2010**, *195*, 2419–2430.
- (5) Thangadurai, V.; Kaack, H.; Weppner, W. *J. F. J. Am. Ceram. Soc.* **2003**, *86*, 437–440.
- (6) Ohta, S.; Kobayashi, T.; Asaoka, T. *J. Power Sources* **2011**, *196*, 3342–3345.
- (7) Rangasamy, E.; Wolfenstine, J.; Sakamoto, J. *Solid State Ionics* **2012**, *206*, 28–32.
- (8) Wang, Y. X.; Lai, W. *Electrochem. Solid-State Lett.* **2012**, *15*, A68–A71.
- (9) Allen, J. L.; Wolfenstine, J.; Rangasamy, E.; Sakamoto, J. *J. Power Sources* **2012**, *206*, 315–319.
- (10) Murugan, R.; Thangadurai, V.; Weppner, W. *Angew. Chem., Int. Ed.* **2007**, *46*, 7778–7781.
- (11) Thangadurai, V.; Weppner, W. *Adv. Funct. Mater.* **2005**, *15*, 107–112.
- (12) Li, Y. T.; Han, J. T.; Wang, C. A.; Xie, H.; Goodenough, J. B. *J. Mater. Chem.* **2012**, *22*, 15357–15361.
- (13) Cussen, E. *J. J. Mater. Chem.* **2010**, *20*, 5167–5173.
- (14) Thangadurai, V.; Adams, S.; Weppner, W. *Chem. Mater.* **2004**, *16*, 2998–3006.
- (15) Adams, S.; Rao, R. P. *J. Mater. Chem.* **2012**, *22*, 1426–1434.
- (16) Xu, M.; Park, M. S.; Lee, J. M.; Kim, T. Y.; Park, Y. S.; Ma, E. *Phys. Rev. B* **2012**, *85*, 052301.
- (17) Miara, L. J.; Ong, S. P.; Mo, Y. F.; Richards, W. D.; Park, Y.; Lee, J. M.; Lee, H. S.; Ceder, G. *Chem. Mater.* **2013**, *25*, 3048–3055.
- (18) Bernstein, N.; Johannes, M. D.; Hoang, K. *Phys. Rev. Lett.* **2012**, *109*, 5.
- (19) Jalem, R.; Yamamoto, Y.; Shiiba, H.; Nakayama, M.; Munakata, H.; Kasuga, T.; Kanamura, K. *Chem. Mater.* **2013**, *25*, 425–430.
- (20) Meier, K.; Laino, T.; Curioni, A. *J. Phys. Chem. C* **2014**, *118*, 6668–6679.
- (21) Wang, Y. X.; Huq, A.; Lai, W. *Solid State Ionics* **2014**, *255*, 39–49.
- (22) Egami, T.; Billinge, S. J. L. *Underneath the Bragg Peaks: Structural Analysis of Complex Materials*, 2nd ed.; Pergamon: Amsterdam, The Netherlands, 2012; pp 1–481.
- (23) Neder, R. B.; Proffen, T. *Diffuse Scattering and Defect Structure Simulations*; Oxford University Press: Oxford, 2008.
- (24) Petkov, V. In *Characterization of Materials*; Kaufmann, E. N., Ed.; John Wiley and Sons: Hoboken, NJ, 2012.
- (25) Tucker, M. G.; Dove, M. T.; Keen, D. A. *J. Appl. Crystallogr.* **2001**, *34*, 630–638.
- (26) Chahid, A.; McGreevy, R. L. *Phys. B* **1997**, *234*, 87–88.
- (27) Keen, D. A.; Stephen, H. *J. Phys.: Condens. Matter* **1998**, *10*, 8217–8234.
- (28) Ohara, K.; Kawakita, Y.; Pusztai, L.; Temleitner, L.; Kohara, S.; Inoue, N.; Takeda, S. *J. Phys.: Condens. Matter* **2010**, *22*, 404203.
- (29) Peterson, P. F.; Gutmann, M.; Proffen, T.; Billinge, S. J. L. *J. Appl. Crystallogr.* **2000**, *33*, 1192–1192.
- (30) Peterson, P. F.; Bozin, E. S.; Proffen, T.; Billinge, S. J. L. *J. Appl. Crystallogr.* **2003**, *36*, 53–64.
- (31) Larson, A. C.; Von Dreele, R. B. *General Structure Analysis System (GSAS)*; Los Alamos National Laboratory Report LAUR 86-748, 2000.
- (32) Toby, B. H. *J. Appl. Crystallogr.* **2001**, *34*, 210–213.
- (33) Tucker, M. G.; Keen, D. A.; Dove, M. T.; Goodwin, A. L.; Hui, Q. *J. Phys.: Condens. Matter* **2007**, *19*, 335218.
- (34) Momma, K.; Izumi, F. *J. Appl. Crystallogr.* **2011**, *44*, 1272–1276.
- (35) *CrystalMaker*; CrystalMaker Software Ltd: Begbroke, Oxfordshire, UK, 2013.
- (36) Smith, W.; Forester, T. R. *J. Mol. Graphics* **1996**, *14*, 136–141.
- (37) Mitchell, P. J.; Fincham, D. *J. Phys.: Condens. Matter* **1993**, *5*, 1031–1038.
- (38) Schnell, S. K.; Liu, X.; Simon, J. M.; Bardow, A.; Bedeaux, D.; Vlugt, T. J. H.; Kjelstrup, S. *J. Phys. Chem. B* **2011**, *115*, 10911–10918.
- (39) Bhattacharya, J.; Van der Ven, A. *Phys. Rev. B* **2010**, *81*, 104304.
- (40) Cussen, E. *J. Chem. Commun.* **2006**, 412–413.
- (41) Han, J. T.; Zhu, J. L.; Li, Y. T.; Yu, X. H.; Wang, S. M.; Wu, G.; Xie, H.; Vogel, S. C.; Izumi, F.; Momma, K.; Kawamura, Y.; Huang, Y.; Goodenough, J. B.; Zhao, Y. S. *Chem. Commun.* **2012**, *48*, 9840–9842.
- (42) Keen, D. A. *J. Appl. Crystallogr.* **2001**, *34*, 172–177.